Research Square

Preprints are preliminary reports that have not undergone peer review.
They should not be considered conclusive, used to inform clinical practice,
or referenced by the media as validated information.

SPARC is associated with vascular smooth muscle cell senescence and vascular remodeling in intracranial aneurysms

Xinlong Ma

19839548960qq.com

Shandong University School of Medicine: Shandong University Cheeloo College of Medicine
https://orcid.org/0009-0000-5614-2751

Lvyin Luo

Shandong University School of Medicine: Shandong University Cheeloo College of Medicine

Xingpeng Zhang

Shandong University School of Medicine: Shandong University Cheeloo College of Medicine

Deibin Kong

Shandong University School of Medicine: Shandong University Cheeloo College of Medicine

Yuxiang Dai

Shandong University School of Medicine: Shandong University Cheeloo College of Medicine

Haoxuan Du

Shandong University School of Medicine: Shandong University Cheeloo College of Medicine

Maogui Li

Shandong University School of Medicine: Shandong University Cheeloo College of Medicine

Yangyang Xu

Shandong University School of Medicine: Shandong University Cheeloo College of Medicine

Tao LI

Shandong University Affiliated Shandong Provincial Third Hospital

Yunyan Wang

Shandong University School of Medicine: Shandong University Cheeloo College of Medicine
https://orcid.org/0000-0003-2507-1625

Research Article

Keywords: intracranial aneurysm, SPARC, vascular smooth muscle cell, cellular senescence, single-cell RNA sequencing, senolytics

Posted Date: November 5th, 2026

DOI: https://doi.org/10.21203/rs.3.rs-11390929/v1

License: This work is licensed under a Creative Commons Attribution 4.0 International License.
Read Full License

Abstract

Background

Intracranial aneurysms (IAs) affect approximately 3% of adults, and no pharmacological therapy is available to stabilize the aneurysm wall. Vascular smooth muscle cell (VSMC) senescence may contribute to IA formation, but its molecular regulators remain unclear. Secreted protein acidic and rich in cysteine (SPARC), a matricellular protein of the FRIDMAN_SENESCENCE_UP gene set, regulates cell–matrix interactions and cell-cycle behavior in vascular smooth muscle. We examined the relationship between SPARC, senescence-associated VSMC states and vascular remodeling in IA.

Methods

Public human IA bulk transcriptomic data (44 IA vs 16 control arteries) were analyzed for differential expression and gene set enrichment, with SPARC validated in three independent cohorts. Single-cell RNA sequencing of eight IA and three superficial temporal artery specimens was integrated to define vascular cell states. SenMayo and VSMC contractility scores were combined into a donor-normalized composite score, and the highest decile within each donor was designated senescence-associated. In mice, *Sparc* deficiency and dasatinib plus quercetin (D + Q) were tested in an elastase-induced IA model (n = 12 per group: sham, IA, *Sparc*-deficient IA, D + Q-treated IA), with additional analyses in aged mice; outcomes were assessed by blinded observers.

Results

SPARC was one of 16 genes shared by IA-upregulated genes and FRIDMAN_SENESCENCE_UP (log2FC = + 1.55, FDR = 0.014). Senescence-associated VSMCs were more frequent in IA samples, with inflammatory features and reduced contractile-gene expression; SPARC expression correlated positively with the SenMayo score (r = [X], P = [X]). In mice, aneurysm incidence was 10/12 (83.3%) in untreated mice versus 3/12 (25.0%) with *Sparc* deficiency (risk ratio [RR] 0.30, 95% CI 0.11–0.83; P = 0.012) and 2/12 (16.7%) with D + Q (RR 0.20, 95% CI 0.06–0.73; P = 0.0033), with reduced senescence staining and preserved contractile markers. In aged mice, *Sparc* deficiency preserved wall structure better, but the lower incidence was not statistically significant (4/12 vs 8/12; RR 0.50, 95% CI 0.19–1.34; P = 0.22).

Conclusions

SPARC is associated with senescence-associated VSMC states and arterial wall remodeling in IA, and *Sparc* deficiency and senolytic treatment were associated with lower aneurysm incidence in mice. Establishing a VSMC-specific mechanism requires further functional validation.

Introduction

Intracranial aneurysms (IAs) are focal dilatations of cerebral arteries that affect approximately 3% of adults [1]. Rupture can cause aneurysmal subarachnoid hemorrhage, a neurological emergency

associated with high mortality and substantial long-term disability. Rebleeding, cerebral vasospasm, and delayed cerebral ischemia further complicate recovery [2, 3].

IA walls exhibit immune cell infiltration, disruption of the internal elastic lamina and medial layer, and extracellular matrix (ECM) remodeling [4, 5]. These changes reflect interactions among hemodynamic stress, genetic susceptibility, hypertension, and inflammation [6]. Preventive treatment relies primarily on microsurgical clipping or endovascular procedures, including coiling and flow diversion. Although these approaches can reduce rupture risk, they carry procedural risks and may require long-term surveillance [7–10]. Understanding the molecular processes that weaken the arterial wall could help identify targets for pharmacological intervention.

Cellular senescence is a state of stable cell-cycle arrest that can develop in response to replicative exhaustion and other forms of cellular stress [11, 12]. Senescent cells often acquire a senescence-associated secretory phenotype (SASP), which can promote inflammation and paracrine senescence [13–15]. Senolytic agents target survival pathways used by some senescent cell populations. Dasatinib plus quercetin (D + Q) is one such combination and has shown beneficial effects in preclinical models of aging [16–18]. Its activity depends on cell type and experimental context; a response to D + Q alone does not establish which senescent population mediates an effect.

VSMC senescence has been implicated in several forms of aneurysmal disease [19]. Senescence-associated changes have been described in abdominal aortic aneurysms and thoracic aortic aneurysm or dissection [20, 21]. VSMCs isolated from abdominal aortic aneurysms also show reduced replicative capacity compared with cells from adjacent arteries [22]. Experimental senolytic treatment can attenuate abdominal aortic aneurysm formation [23], and interventions targeting senescence-associated pathways may improve VSMC phenotypes in other vascular diseases [24]. DNA damage, inflammatory signaling, and reduced expression of contractile genes provide plausible links between VSMC senescence and arterial wall degeneration [25–28]. Whether comparable processes are regulated by SPARC in IAs requires further investigation.

SPARC is a matricellular glycoprotein involved in cell–matrix interactions and tissue remodeling. Altered SPARC expression has been reported in autosomal dominant polycystic kidney disease (ADPKD) [29], a condition associated with an increased prevalence of IA [30]. SPARC can alter cell-cycle regulation in cultured arterial smooth muscle cells [31], and studies in cardiovascular and adipose tissues have linked it to inflammation and aging-associated remodeling [32–34]. SPARC is also included in the FRIDMAN_SENESCENCE_UP gene set [35]. Prior studies directly linked SPARC to autophagy-associated phenotypic modulation, HK2-associated apoptosis, and macrophage-like phenotypic changes in VSMCs in the context of IA [36–38]. Here, we integrated bulk and single-cell transcriptomic analyses with genetic and pharmacological interventions in mice to investigate the relationship between SPARC, senescence-associated VSMC states, and IA wall remodeling.

Results

Senescence related transcriptional features in human intracranial aneurysms

SPARC is a senescence-associated gene up-regulated in intracranial aneurysm. Volcano plot of differentially expressed genes in GSE122897 (44 intracranial aneurysms vs 16 control intracranial arteries). Red and green triangles denote up- and down-regulated genes; SPARC is highlighted (log_2FC = + 1.55, FDR = 0.014, adjusted for sex and age) (Fig. 1A). Intersection of up-regulated genes with the FRIDMAN_SENESCENCE_UP gene set yielded 16 senescence-associated candidate genes (listed on the right) (Fig. 1B). STRING protein–protein interaction network of the 16 candidates (Homo sapiens, combined score ≥ 0.4; 16 nodes, 48 edges). Node size represents degree and node fill represents maximal clique centrality (MCC); SPARC is outlined in red. Node borders indicate community assignment (dark blue, ECM/remodeling; green, cell-cycle/inflammation; purple, no interaction ≥ 0.4) (Fig. 1C). Validation of SPARC expression in three independent datasets: GSE122897 (RNA-seq, 44 vs 16; Mann-Whitney U), GSE75436 (Affymetrix HG-U133 Plus 2.0, 15 aneurysms vs 15 paired superficial temporal arteries from the same patients (Fig. 1D); Wilcoxon signed-rank test) and GSE54083 (Agilent, 13 vs 10; Mann-Whitney U). Bars, mean; error bars, SEM; dots, individual samples; ***P < 0.001. GSEA of samples ranked by SPARC expression (Fig. 1E) (left, low SPARC; right, high SPARC), showing significant negative enrichment of epithelial–mesenchymal transition and the p53 pathway in SPARC-high samples. Hallmark pathway enrichment of up-regulated (left) and down-regulated (right) genes; dot size indicates gene count and color indicates $-log_{10}(P)$. KEGG pathway–gene chord diagram (Fig. 1F,G).

SenMayo scores characterize senescence associated transcriptional differences

We compared several gene sets related to senescence, including FRIDMAN_SENESCENCE_UP, SenMayo, the p53 pathway, GenAge, and a cellular senescence gene set. The SenMayo and FRIDMAN_SENESCENCE_UP profiles showed enrichment toward IA samples in the displayed GSEA results (Fig. 2A). Higher SenMayo scores were associated with an inflammatory response signature, whereas lower scores were associated with myogenesis (Fig. 2B). The displayed p53 and G2M checkpoint results did not reach a nominal P value below 0.05. Receiver operating characteristic (ROC) analyses were used to examine discrimination between IA and control tissue samples (Fig. 2C); this analysis evaluates disease-group discrimination and does not directly validate measurement of cellular senescence or prediction of future IA development. SPARC expression correlated positively with the SenMayo score (Fig. 2D). In the mouse transcriptomic analysis, 118 genes were upregulated and 96 were downregulated in the IA group relative to the sham group (Fig. 2E). Functional analysis identified p53-related features among upregulated genes and KRAS_SIGNALING_DN among downregulated genes (Fig. 2F).

Single cell analysis identifies changes in vascular and immune cell composition

The integrated single-cell dataset comprised eight IA samples and three superficial temporal artery (STA) samples. Following quality control and integration, cells were assigned to nine major populations using established marker expression patterns: VSMCs (MYH11, ACTA2, MYL9, and TAGLN), T and natural killer cells (CD3E, TRAC, TRBC2, and NKTR), monocytes and macrophages (CSF1R, CD14, and CD68), neutrophils (S100A9, CSF3R, and FCGR3B), dendritic cells (CD74, HLA-DQA1, and IRF8), endothelial cells (PECAM1, VWF, CDH5, and KDR), fibroblasts (DCN and PDGFRA), Schwann cells (MPZ, PLP1, and PMP22), and mast cells (MS4A2, KIT, CMA1, TPSB2, and FCER1A). UMAP embeddings and marker expression plots summarized these populations (Fig. 3A–D). IA samples showed higher pooled proportions of T/NK cells, neutrophils, fibroblast, and monocytes/macrophages, together with lower proportions of VSMCs and endothelial cells (Fig. 3E,F). These pooled proportions describe the recovered cells and do not establish donor-level differences in cell abundance.

The VSMC subset contained 26,073 cells, including 17,605 from IA samples and 8,468 from STA samples (Fig. 4A). Marker programs related to inflammation (LGALS1, CMSS1, and S100A4), migration (NFKB1, NEAT1, and GPC6), ECM production (SPP1, SERPINF1, and TNFRSF11B), and contractility (MYH11, CNN1, and ACTA2) were used to describe five VSMC states: migratory/contractile (Mig/Con), ECM-producing/inflammatory (ECM/Inf), contractile/inflammatory (Con/Inf), contractile (Con), and inflammatory with low contractility (Inf/LackCon; Fig. 4B,C,E). IA samples contained a higher proportion of cells assigned to Inf/LackCon and ECM/Inf states and a lower proportion assigned to the Con state (Fig. 4D).

The SenMayo senescence gene set (125 genes;[50]) and a VSMC contractility gene set (132 genes genes;[51]) (Fig. 4F) were used for scoring. The complete gene lists and the number of genes detected per dataset are provided in Supplementary Table 2. Gene set activity was quantified per cell with AUCell (version 1.26.0) using the ranking-based AUC, with aucMaxRank set to 0.05. Because AUC values are bounded by gene set size and the two sets differ in size, absolute AUC values were not compared between sets; instead, each score was r z-standardised within each donor before further use. Scores were computed on assay of the QC-passed VSMC subset.

We defined a "senescence-contractility composite score" for each cell, calculated as the donor-normalized SenMayo score minus the donor-normalized contractility score. Within each donor, we ranked VSMCs by this composite score, and defined the top 10% of VSMCs with the highest composite score as senescence-associated VSMCs (primary definition, 10% threshold) (Fig. 4G). This operational definition is designed to identify a specific transcriptional state, and does not by itself confirm that the cells are in irreversible senescence. These cells were more frequent in IA samples and were concentrated within the ECM/Inf state, with a smaller fraction in the Inf/LackCon state (Fig. 4H,I).

Senescence-associated VSMCs showed increased expression of genes including COMP, LRRC15, GREM1, KCNK2, and STEAP1, together with reduced expression of contractile genes such as MYH11 and PLN (Fig. 5A). Functional analysis associated upregulated genes with TNF signaling and related inflammatory pathways, whereas downregulated genes were associated with vascular smooth muscle contraction (Fig. 5B). CellChat inferred differences in communication networks across VSMC states, including interactions involving CXCL12–ACKR3 and distinct outgoing and incoming signaling patterns (Fig. 5C–E). These predictions identify candidate intercellular interactions rather than experimentally established signaling mechanisms. Cell-cycle scoring assigned a greater fraction of senescence-associated VSMCs to G1 and a smaller fraction to G2/M than the remaining VSMCs (Fig. 5F). SPARC expression was positively associated with the senescence-contractility composite score (Fig. 5G-H).

Sparc deficiency and senolytic treatment are associated with reduced arterial wall damage

The mouse IA model combined carotid and renal artery ligation, an 8% NaCl diet, and stereotactic elastase injection into the basal cistern one week after ligation. Cerebral arteries were examined one month after elastase injection (Fig. 6A). Four groups were compared (n = 12 mice per group): sham-operated mice, wild-type mice with induced IA, Sparc-deficient mice with induced IA, and mice receiving D + Q during IA induction. Aneurysm occurrence was 10/12 (83.3%, 95% CI 55.2–95.3%) in untreated IA mice, compared with 0/12 (0%, 0–24.3%) in sham mice, 3/12 (25.0%, 8.9–53.2%) in Sparc-deficient mice and 2/12 (16.7%, 4.7–44.8%) in D + Q-treated mice (Fisher's exact test versus untreated IA: $P = 6.7 \times 10^{-5}$, 0.012 and 0.0033, respectively; Holm-adjusted $P = 2.0 \times 10^{-4}$, 0.012 and 0.0067). Gross vascular examination and hematoxylin and eosin (H&E), Masson's trichrome, and elastin staining showed less arterial wall disruption in the Sparc-deficient and D + Q groups than in the untreated IA group. Senescence-associated β-galactosidase (SA-β-gal) staining was also reduced (Fig. 6B,C). Immunofluorescence images showed lower CDKN2A/p16 and CDKN1A/p21 signals and greater preservation of the contractile markers MYH11 and ACTA2 in both intervention groups (Fig. 6D,E). Quantitative summaries (n = 12 mice per group) showed lower elastin degradation scores, lower collagen-to-muscle ratios and greater medial thickness in these groups (Fig. 6F). These findings support an association between the interventions and preservation of arterial wall structure and VSMC phenotype.

Discussion

This study combined human transcriptomic analyses with mouse experiments to examine the relationship between SPARC, senescence-associated VSMC states, and IA remodeling. Human IA samples contained VSMCs with inflammatory transcriptional features and reduced contractile-gene expression, and SPARC expression was positively associated with the SenMayo score. In mice, Sparc deficiency and D + Q treatment were associated with less arterial wall degeneration and lower

senescence-associated staining. Similar structural findings in aged Sparc-deficient mice suggest that the relationship extends to an aging context.

The contribution of this study should be considered alongside previous work on SPARC in vascular disease. SPARC has been linked to arterial smooth muscle cell-cycle regulation [31], and its expression varies in metabolic and inflammatory settings [39–41]. Direct studies in brain VSMCs have already implicated SPARC in AMPK/mTOR-mediated autophagy and phenotypic modulation [36], HK2-associated apoptosis [37], and ROS-associated macrophage-like phenotypic transformation [38]. The present study extends this work by examining senescence-associated cell states at single-cell resolution and by assessing vascular phenotypes after Sparc deletion and senolytic treatment in vivo. It does not establish that SPARC–IA associations are unique to senescence or that SPARC expression alone predicts clinical outcomes.

The transcriptomic analyses connect SPARC expression with a broader remodeling program. SPARC was one of 16 genes shared by the IA-upregulated gene set and FRIDMAN_SENESCENCE_UP. SenMayo scoring also captured transcriptional differences between IA and control tissues. However, bulk-tissue scores are influenced by cell composition, inflammation, and the anatomical source of control arteries. The ROC analyses evaluate the separation of existing disease groups; they do not establish a prospective biomarker of aneurysm formation, progression, or rupture. Such applications would require independent cohorts, appropriate clinical comparators, and longitudinal validation.

Single-cell analysis localized senescence-associated transcriptional features to VSMC states with inflammatory and ECM-related programs. The composite SenMayo-minus-contractility score offers a way to prioritize cells for further investigation, but it also introduces a dependence between group definition and downstream findings. Reduced contractile-gene expression and higher SenMayo scores cannot independently validate a group selected using those same features. Similarly, G1 assignment from transcriptomic cell-cycle scores cannot distinguish irreversible senescence from quiescence. CellChat predictions, including CXCL12–ACKR3 interactions, suggest possible communication pathways that require direct functional testing.

The mouse experiments provide complementary evidence that Sparc deficiency and D + Q treatment are associated with preservation of the aneurysmal arterial wall. Reduced SA-β-gal and p16/p21 staining is consistent with attenuation of senescence-associated changes, while preservation of MYH11 and ACTA2 supports a more contractile molecular phenotype. These staining results do not measure vascular contractile function directly. In addition, the similar effects of Sparc deletion and D + Q do not establish that both interventions act through the same pathway or that D + Q selectively targets senescent VSMCs in this model.

The transcriptomic and ultrastructural findings in Sparc-deficient mice suggest an association with preserved structural programs and reduced inflammatory remodeling. Myogenesis, muscle cytoskeleton, and ECM–receptor interaction signatures were relatively increased in the knockout group, while inflammatory and IL-17-related signatures were associated with the IA group. Because the RNA

sequencing used whole arterial tissue, these changes may reflect both altered cellular states and differences in tissue composition. Electron microscopy provides structural support but does not, on its own, establish changes in apoptosis, mitochondrial function, or contractile performance.

Several limitations should guide interpretation. The human single-cell cohort is small, and IA and STA specimens differ in anatomical origin. Age, sex, rupture status, comorbidities, and processing batch may influence the observed differences. Donor-level replication is essential because individual cells from the same donor are not independent biological replicates. The score-based VSMC definition requires validation using independent senescence measures and alternative thresholds. Global Sparc deficiency cannot identify the responsible cell type, and effects on blood pressure or other systemic factors could influence aneurysm formation. Cell-specific loss- and gain-of-function experiments and rescue studies would help determine whether VSMC senescence mediates the vascular phenotype. Finally, prevention during experimental IA induction does not establish efficacy against existing aneurysms or support clinical use of senolytic therapy.

Together, these findings associate SPARC with senescence-related VSMC states and arterial wall remodeling in IA. The mouse data support further investigation of SPARC as a candidate regulator of aneurysmal remodeling. Establishing a direct VSMC-specific mechanism and validating the observed effects with complete quantitative and functional measurements are necessary before drawing therapeutic conclusions.

Methods

Human tissue samples

IA tissue was obtained from six patients undergoing microsurgical clipping at Qilu Hospital, Shandong University, for single-cell RNA sequencing. Clinical information is described in Supplementary File 1. These data were combined with previously generated single-cell datasets from two IA and three STA samples [52], yielding eight IA and three STA samples in total. The newly generated and previously generated data are deposited in the Genome Sequence Archive for Human (GSA-Human), National Genomics Data Center (https://ngdc.cncb.ac.cn/gsa-human/), under accession numbers HRA014414 (6IAs) and HRA007438 (2IAs and 3STAs), respectively. Human tissue collection was approved by the Ethics Committee of Qilu Hospital, Shandong University (KYLL-2024(ZM)-428), and informed consent was obtained.

Mice

In the first experiment: 6-week-old male C57BL/6J mice were purchased from Beijing Weitonghe Laboratory Animal Technology Co., Ltd., and 6-week-old Sparc gene-deficient mice were bred by Beijing Weisuolide Biotechnology Co., Ltd. After 2 weeks of adaptive feeding, mice were subjected to intracranial aneurysm model construction.

In the second age-gradient experiment: 18-month-old aged male C57BL/6J mice were purchased from Beijing Weitonghe Laboratory Animal Technology Co., Ltd.; 18-month-old aged Sparc gene-deficient mice were obtained by continuously feeding the 6-week-old Sparc gene-deficient mice to 18 months of age.

All experimental mice were housed in a Specific Pathogen Free (SPF) animal facility with constant temperature and humidity, and maintained on a 12-hour light/12-hour dark cycle. The construction and identification of Sparc gene-deficient mouse genotypes were completed by Beijing Weisuolide Biotechnology Co., Ltd. All animal experimental procedures in this study were approved by the Experimental Animal Ethics Committee of Qilu Hospital of Shandong University (Approval No. DWLL-2024-235), and strictly performed in accordance with the Guide for the Care and Use of Laboratory Animals.

Elastin staining and degradation scoring

Paraffin sections approximately 5 μm thick were deparaffinized and stained using an elastin staining kit (G1042, Servicebio) according to the manufacturer's instructions. At least five sections were examined per animal. Images were acquired using the WISLEAP Multimodal Scanning System (WISLEAP Medical Technology, Suzhou, China). Elastin disruption was assessed microscopically at 80× magnification.

Elastin degradation scoring. Elastin integrity was assessed on elastin–van Gieson (EVG)-stained sections using a four-point scale adapted from a published method [20]: 1, no degradation; 2, mild degradation with focal internal elastic lamina (IEL) interruptions or breaks; 3, moderate degradation with numerous IEL breaks; and 4, severe degradation with extensive loss of elastic fibers or wall rupture. Because intracranial arteries possess a prominent IEL and lack a well-developed external elastic lamina, the scale was applied to the IEL and adjacent media of cerebral arteries, and the descriptors were adjusted accordingly; the adapted scale was pre-tested on cerebral artery sections, and inter-observer agreement was assessed by Cohen's weighted kappa. For each animal, at least five EVG-stained sections spanning the Circle of Willis and the proximal major cerebral arteries were scored, and each section was assessed in at least three repeated measurements. Repeated measurements within a section were averaged to give a single section value, and section values were then aggregated to one animal-level score (median of section values). Sections and repeated measurements were technical replicates and were never treated as independent observations. Two observers blinded to group allocation performed all assessments independently.

H&E staining and Measurement of medial smooth muscle layer thickness.

Cerebral arteries were fixed in 4% paraformaldehyde at 4 °C overnight, dehydrated through a graded ethanol series, cleared in xylene and embedded in paraffin. Cross-sections (4 μm) were cut, deparaffinized, rehydrated, stained with Harris haematoxylin (5 min) and eosin (2 min), dehydrated,

cleared and mounted. Images were acquired under identical exposure settings with a microscope, ×40 objective.

Medial thickness was measured on H&E cross-sections of the parent artery adjacent to the aneurysm (the aneurysm dome and branch points were avoided). For each section, the distance between the inner and outer borders of the media was measured perpendicular to the long axis of the vessel at four equidistant quadrants using ImageJ/Fiji, with the scale calibrated against a stage micrometer before each session. Measurements were repeated at least three times per section and averaged; section means were then averaged to give a single value per animal. Observers were blinded to group allocation.

All comparisons were performed at the animal level (n = 12 per group); histological sections and repeated measurements were technical replicates and were not used as independent observations. Data are presented as mean ± SD. Continuous variables were compared by the Independent-samples t tests; aneurysm incidence was compared by Fisher's exact test.

Masson trichrome staining

Deparaffinized sections were stained with Masson’s trichrome reagent (G1006-20ML, Servicebio) according to the manufacturer’s instructions and imaged using the WISLEAP system. The ratio of collagen-positive area (blue) to muscle-positive area (red) in the basal cerebral arterial wall was measured using ImageJ (version 1.5.3).

Senescence associated beta galactosidase staining

SA-β-gal staining was performed on basal cerebral arteries using a β-galactosidase staining kit (G3060-100ML, Solarbio). Samples were washed three times with phosphate-buffered saline (PBS), fixed with formaldehyde for 15 minutes, and incubated with the staining solution overnight at 37 °C without CO_2. Samples were then washed with PBS and imaged using the WISLEAP system.

Images were analyzed in ImageJ/Fiji by observers blinded to group allocation. The vessel wall was defined as the region of interest (ROI) on the corresponding H&E or EVG image of the same segment. SA-β-gal-positive signal was segmented in the hue/saturation channels using fixed thresholds applied identically to all images, and the result was expressed as the percentage of positive area within the vessel wall ROI (positive area / total vessel wall area × 100%). For each animal, at least five vessel segments were imaged and each segment was measured in at least three repeated measurements; repeated measurements were averaged to give one value per segment, and segment values were aggregated to a single animal-level value (mean). Segments and repeated measurements were technical replicates and were not treated as independent observations; all comparisons were performed at the animal level (n = 12 per group).

Immunofluorescence

Paraffin sections were heated at 70 °C for 30 minutes, deparaffinized with xylene, processed with ethanol, and washed three times with PBS. Antigen retrieval was performed in EDTA solution (0085, Beyotime) at 95 °C for 30 minutes, followed by cooling to room temperature for 1 hour. Frozen sections were washed directly with PBS. Sections were treated with 3% H_2O_2 for 10 minutes and blocked for 30 minutes in a solution containing 0.5% Triton X-100, 1% bovine serum albumin, and 10% serum. Primary antibodies were applied at dilutions of 1:100–1:500 overnight at 4 °C or for 1–2 hours at room temperature. Following three PBS washes of 3 minutes each, sections were incubated with FITC- or Cy3-labeled secondary antibodies at dilutions of 1:500–1:1,000 for 1–2 hours at room temperature in the dark. After three further PBS washes, sections were mounted and stored at 4 °C in the dark until fluorescence imaging.

Mouse intracranial aneurysm model

IA induction was based on previously described approaches [42,43]. The left renal artery was ligated, and mice received an 8% NaCl diet (XTNacl-8C, Jiangsu Xietong, Nanjing, China). The left common carotid artery was also ligated to alter intracranial hemodynamics. One week later, elastase was injected stereotactically into the right basal cistern. One month after elastase injection, the cerebral vasculature was perfused with bromophenol blue–gelatin solution, and the circle of Willis was examined for focal arterial protrusions. Two investigators assessed vascular morphology independently while blinded to group allocation.

The first experiment included four groups. Sham-operated mice underwent exposure of the carotid and renal arteries without ligation, received basal cistern saline injection, and were maintained on the 8% NaCl diet. Wild-type IA mice underwent the full induction procedure. Sparc-deficient IA mice underwent the same induction procedure. The senolytic group underwent IA induction and received oral dasatinib (12 mg/kg) plus quercetin (50 mg/kg) three times per week during the induction period.

The second experiment compared aged wild-type C57BL/6J mice and aged Sparc-deficient mice subjected to the same IA induction procedure.

Animals were randomly assigned to experimental groups. Investigators assessing outcomes were blinded to genotype and treatment allocation.

Mouse arterial RNA sequencing

Basal cerebral arteries, including the basilar artery and vessels of the circle of Willis, were dissected under a microscope and immediately stored in liquid nitrogen. Three independent animals per group (sham-operated wild-type, wild-type IA and Sparc-deficient IA) were sequenced; samples were not

pooled. RNA library preparation, sequencing and bioinformatic analysis were performed by Hangzhou Lianchuan Biotechnology Co., Ltd. (LC-Bio, Hangzhou, China).

Public transcriptomic datasets

Human bulk gene expression datasets GSE122897 [44], GSE54083 [45], and GSE75436 [46] were obtained from the Gene Expression Omnibus (GEO). GSE122897 compares IA tissue with control intracranial cortical arteries; the STA controls described above refer to the single-cell cohort. Dataset characteristics are described in Supplementary File 1.

Differential expression and functional enrichment analysis

Differential expression analysis of GSE122897 was performed using limma (version 3.60.6). The stated selection criteria were an absolute $\log_2$ fold change greater than 1 and a false discovery rate (FDR)-adjusted P value below 0.05. IA-upregulated DEGs were intersected with the FRIDMAN_SENESCENCE_UP gene set. Heatmaps were generated using pheatmap (version 1.0.12).

GO and KEGG analyses were performed using clusterProfiler (version 4.12.6). Hallmark gene sets and GSEA were used to characterize transcriptional programs. The stated gene set size limits were 5–5,000 genes. The GSEA criteria were an absolute normalized enrichment score greater than 1, a nominal P value below 0.05, and an FDR q value below 0.20. Enrichment patterns not meeting these criteria were interpreted as exploratory.

Single cell library preparation and sequencing

Fresh tissue was washed in precooled sterile PBS, transferred to preservation solution, and transported on ice. Samples were digested at 37 °C for 1 hour, filtered, and centrifuged. After red blood cell lysis, the reaction was stopped and cells were resuspended at 2×10^5 cells/mL. Cell suspensions were loaded onto microwell chips using the Singleron Matrix system. Barcoding beads were collected for reverse transcription and cDNA amplification. Libraries were prepared using the GEXSCOPE workflow, pooled, and sequenced on an Illumina NovaSeq 6000 instrument.

Raw reads were processed with CeleScope (version 1.9.0). Low-quality sequences, poly(A) tails, and adapters were removed using Cutadapt (version 1.17), and cell barcodes and unique molecular identifiers (UMIs) were extracted. Reads were aligned to the GRCh38 reference genome with Ensembl release 92 annotation using STAR (version 2.6.1a) [47]. featureCounts (version 2.0.1) was used in generating gene expression matrices for downstream analysis.

Cells were excluded if they had more than 30,000 UMIs, fewer than 200 or more than 6,000 detected genes, or mitochondrial transcript fractions above 30%. Downstream analyses used Seurat (version

5.2.1) [48] in R (version 4.4.3). Expression data were processed using NormalizeData and ScaleData, and the 2,000 most variable genes were selected using FindVariableFeatures for principal component analysis. The first 20 principal components were used in downstream analysis. Harmony [49] was applied to account for sample-associated batch effects. Cells were clustered using FindClusters and visualized using UMAP.

Cell annotation and VSMC state scoring

The integrated analysis included six newly sequenced IA samples and the previously generated datasets from two IA and three STA samples. Major cell populations were annotated using marker expression and the CellMarker 2.0 database.

VSMCs were extracted and further characterized using marker programs related to inflammation (LGALS1, CMSS1, and S100A4), migration (NFKB1, NEAT1, and GPC6), ECM production (SPP1, SERPINF1, and TNFRSF11B), and contractility (MYH11, CNN1, and ACTA2). The resulting states were designated Mig/Con, ECM/Inf, Con/Inf, Con, and Inf/LackCon.

AUCell (version 1.26.0) was used to score VSMCs with the SenMayo gene set [50] and a VSMC contractility gene set [51]. A composite score was calculated by subtracting the contractility score from the SenMayo score. VSMCs in the highest decile of the composite score were designated senescence-associated VSMCs. Differential expression, functional enrichment, cell-cycle scoring, and CellChat analyses were used to characterize these cells and the remaining VSMC states.

Gene set variation analysis

Sample-level gene set enrichment scores were calculated using the GSVA R package (version 1.40.1). These scores were used to compare transcriptional programs across samples and to evaluate their associations with disease group.

ROC analysis

ROC curves were constructed from sample-level SenMayo scores to assess discrimination between IA and control tissues. The area under the ROC curve (AUC) summarized discrimination across classification thresholds.

ROC results were interpreted as measures of disease-group discrimination. AUC magnitude alone was not treated as a statistical significance test or as evidence that the score measures the extent of cellular senescence.

Statistical analysis

Statistical analyses used GraphPad Prism (version 9.0) and R (version 4.4.3). Image-based measurements were obtained with ImageJ (version 1.5.3). Independent-samples t tests were used for the reported two-group comparisons. Quantitative results are expressed as mean ± standard deviation (SD).

A P value below 0.05 was considered statistically significant, except where the stated multiple-testing criteria applied.

Declarations

Funding

This work was supported by the Natural Science Foundation of Shandong Province (ZR2022MH263), the China Foundation for International Science Exchange (Z2018LSD001), and the Qilu Zhongke New Kinetic Energy Innovation Research Institute (6010123142).

Ethics approval and consent to participate

Human research was approved by the Ethics Committee of Qilu Hospital, Shandong University (KYLL-2024(ZM)-428), and conducted in accordance with the Declaration of Helsinki. Informed consent for tissue use was obtained from participants or their guardians. Animal experiments were approved by the Laboratory Animal Ethics Committee of Qilu Hospital, Shandong University (DWLL-2024-235) and conducted in accordance with the Guide for the Care and Use of Laboratory Animals (National Research Council, 2011).

Availability of data and materials

The public bulk transcriptomic datasets are available in GEO under accession numbers GSE122897, GSE54083, and GSE75436. The newly generated and previously generated data are deposited in the Genome Sequence Archive for Human (GSA-Human), National Genomics Data Center (https://ngdc.cncb.ac.cn/gsa-human/), under accession numbers HRA014414 (6IAs) and HRA007438 (2IAs and 3STAs), respectively. Mouse RNA sequencing data and analytical pipelines are available from the corresponding author upon reasonable request.

Competing interests

The authors declare no competing interests.

References

1. Vlak MHM, Algra A, Brandenburg R, Rinkel GJE. Prevalence of unruptured intracranial aneurysms, with emphasis on sex, age, comorbidity, country, and time period: a systematic review and meta-analysis. Lancet Neurol. 2011;10(7):626–36. 10.1016/S1474-4422(11)70109-0.
2. Neifert SN, et al. Aneurysmal Subarachnoid Hemorrhage: the Last Decade. Transl Stroke Res. 2021;12(3):428–46.
3. Overstijns M et al. Clinical severity of aneurysmal subarachnoid hemorrhage over time: systematic review. 2024. 47(1): p. 257.
4. Zhong W, et al. Aneurysm Wall Enhancement in Unruptured Intracranial Aneurysms: A Histopathological Evaluation. J Am Heart Assoc. 2021;10(2):e018633.
5. Brisman JL, Song JK, Newell DW. Cerebral aneurysms. N Engl J Med. 2006;355(9):928–39.
6. Frösen J, et al. Flow-induced, inflammation-mediated arterial wall remodeling in the formation and progression of intracranial aneurysms. Neurosurg Focus. 2019;47(1):E21.
7. Ramirez-Velandia F, et al. Timing, type, and impact of thromboembolic events caused by flow diversion: a 10-year experience. J Neurosurg. 2025;142(1):78–87.
8. Kotowski M, et al. Safety and occlusion rates of surgical treatment of unruptured intracranial aneurysms: a systematic review and meta-analysis of the literature from 1990 to 2011. J Neurol Neurosurg Psychiatry. 2013;84(1):42–8.
9. Naggara ON, et al. Endovascular treatment of intracranial unruptured aneurysms: a systematic review of the literature on safety with emphasis on subgroup analyses. Radiology. 2012;263(3):828–35.
10. Mertens R, et al. Role of clipping in aneurysmal subarachnoid hemorrhage: a post hoc analysis of the Earlydrain trial. Neurosurg Rev. 2024;47(1):824.
11. Hayflick L, Moorhead PS. The serial cultivation of human diploid cell strains. Exp Cell Res. 1961;25:585–621.
12. Gorgoulis V, et al. Cellular Senescence: Defining a Path Forward. Cell. 2019;179(4):813–27.
13. Schnabl B, et al. Replicative senescence of activated human hepatic stellate cells is accompanied by a pronounced inflammatory but less fibrogenic phenotype. Hepatology. 2003;37(3):653–64.
14. Chi C, et al. Vascular smooth muscle cell senescence and age-related diseases: State of the art. Biochim Biophys Acta Mol Basis Dis. 2019;1865(7):1810–21.
15. Acosta JC, et al. A complex secretory program orchestrated by the inflammasome controls paracrine senescence. Nat Cell Biol. 2013;15(8):978–90.
16. Xu M, et al. Senolytics improve physical function and increase lifespan in old age. Nat Med. 2018;24(8):1246–56.

17. Kirkland JL, Tchkonia T. Senolytic drugs: from discovery to translation. J Intern Med. 2020;288(5):518–36.
18. Zhu Y, et al. The Achilles' heel of senescent cells: from transcriptome to senolytic drugs. Aging Cell. 2015;14(4):644–58.
19. Lin MJ, et al. Targeting Vascular Smooth Muscle Cell Senescence: A Novel Strategy for Vascular Diseases. J Cardiovasc Transl Res. 2023;16(5):1010–20.
20. Chen HZ, et al. Age-Associated Sirtuin 1 Reduction in Vascular Smooth Muscle Links Vascular Senescence and Inflammation to Abdominal Aortic Aneurysm. Circ Res. 2016;119(10):1076–88.
21. Zhang WM, et al. Sustained activation of ADP/P2ry12 signaling induces SMC senescence contributing to thoracic aortic aneurysm/dissection. J Mol Cell Cardiol. 2016;99:76–86.
22. Liao S, et al. Accelerated replicative senescence of medial smooth muscle cells derived from abdominal aortic aneurysms compared to the adjacent inferior mesenteric artery. J Surg Res. 2000;92(1):85–95.
23. Xie J, et al. Clearance of Stress-Induced Premature Senescent Cells Alleviates the Formation of Abdominal Aortic Aneurysms. Aging Dis. 2023;14(5):1778–98.
24. Sung JY et al. Telomere stabilization by metformin mitigates the progression of atherosclerosis via the AMPK-dependent p-PGC-1α pathway. Exp Mol Med, 2024.
25. Liu Z-L, et al. Aging aggravates aortic aneurysm and dissection via miR-1204-MYLK signaling axis in mice. Nat Commun. 2024;15(1):5985.
26. Uryga AK, et al. Telomere damage promotes vascular smooth muscle cell senescence and immune cell recruitment after vessel injury. Commun Biol. 2021;4(1):611.
27. Gao P, et al. MKL1 cooperates with p38MAPK to promote vascular senescence, inflammation, and abdominal aortic aneurysm. Redox Biol. 2021;41:101903.
28. Jia LX, et al. Mechanical stretch-induced endoplasmic reticulum stress, apoptosis and inflammation contribute to thoracic aortic aneurysm and dissection. J Pathol. 2015;236(3):373–83.
29. Wang W, et al. Aberrant expression of SPARC and its impact on proliferation and apoptosis in ADPKD cyst-lining epithelia. Nephrol Dial Transpl. 2006;21(5):1278–88.
30. Flahault A, et al. Screening for intracranial aneurysms in autosomal dominant polycystic kidney disease is cost-effective. Kidney Int. 2018;93(3):716–26.
31. Ye GF, et al. Secreted Protein Acidic and Rich in Cysteine Modulates Molecular Arterial Homeostasis of Human Arterial Smooth Muscle Cells In Vitro. J Mol Neurosci. 2016;60(4):509–16.
32. Toba H, Takai S. Exploring the roles of SPARC as a proinflammatory factor and its potential as a novel therapeutic target against cardiovascular disease. Am J Physiol Heart Circ Physiol. 2024;327(5):H1174–86.
33. Whytock KL, et al. Aging human abdominal subcutaneous white adipose tissue at single cell resolution. Aging Cell. 2024;23(11):e14287.

34. Ryu S, et al. The matricellular protein SPARC induces inflammatory interferon-response in macrophages during aging. Immunity. 2022;55(9):1609–e16267.
35. Fridman AL, Tainsky MA. Critical pathways in cellular senescence and immortalization revealed by gene expression profiling. Oncogene. 2008;27(46):5975–87.
36. Li T, et al. SPARC induces phenotypic modulation of human brain vascular smooth muscle cells via AMPK/mTOR-mediated autophagy. Neurosci Lett. 2019;712:134485. 10.1016/j.neulet.2019.134485.
37. Zhou D, et al. Secreted protein acidic and rich in cysteine (SPARC) induces apoptosis of human brain vascular smooth muscle cells through regulating HK2 in intracranial aneurysm. Front Mol Neurosci. 2023;16:1290556. 10.3389/fnmol.2023.1290556.
38. Ye G, et al. SPARC modulates macrophage-like phenotype transformation in VSMCs and triggers a vicious cycle. Front Cell Dev Biol. 2026;14:1791698. 10.3389/fcell.2026.1791698.
39. Tsurudome Y, et al. Increased SPARC in brain microvessels of ob/ob mice accelerates molecular transport into the brain accompany with albumin. Life Sci. 2024;355:122990.
40. Kos K, Wilding JP. SPARC: a key player in the pathologies associated with obesity and diabetes. Nat Rev Endocrinol. 2010;6(4):225–35.
41. Takahashi M, et al. The expression of SPARC in adipose tissue and its increased plasma concentration in patients with coronary artery disease. Obes Res. 2001;9(7):388–93.
42. Nuki Y, et al. Elastase-induced intracranial aneurysms in hypertensive mice. Hypertension. 2009;54(6):1337–44.
43. Makino H, et al. Pharmacological stabilization of intracranial aneurysms in mice: a feasibility study. Stroke. 2012;43(9):2450–6.
44. Kleinloog R, et al. Sequencing Analysis of Intracranial Aneurysm Walls Reveals Involvement of Lysosomes and Immunoglobulins in Rupture. Stroke. 2016;47(5):1286–93.
45. Pera J, et al. Gene expression profiles in human ruptured and unruptured intracranial aneurysms: what is the role of inflammation? Stroke. 2010;41(2):224–31.
46. Yu L, et al. Gene expression profiles in intracranial aneurysms. Neurosci Bull. 2014;30(1):99–106.
47. Dobin A, et al. STAR: ultrafast universal RNA-seq aligner. Bioinformatics. 2013;29(1):15–21.
48. Satija R, et al. Spatial reconstruction of single-cell gene expression data. Nat Biotechnol. 2015;33(5):495–502.
49. Korsunsky I, et al. Fast, sensitive and accurate integration of single-cell data with Harmony. Nat Methods. 2019;16(12):1289–96.
50. Saul D, et al. A new gene set identifies senescent cells and predicts senescence-associated pathways across tissues. Nat Commun. 2022;13(1):4827.
51. Luo Y, et al. The activator protein-1 complex governs a vascular degenerative transcriptional programme in smooth muscle cells to trigger aortic dissection and rupture. Eur Heart J. 2024;45(4):287–305.

52. Luo L, et al. Multiomics integrated analysis and experimental validation identify TLR4 and ALOX5 as oxidative stress-related biomarkers in intracranial aneurysms. J Neuroinflammation. 2024;21(1):225.

Figures

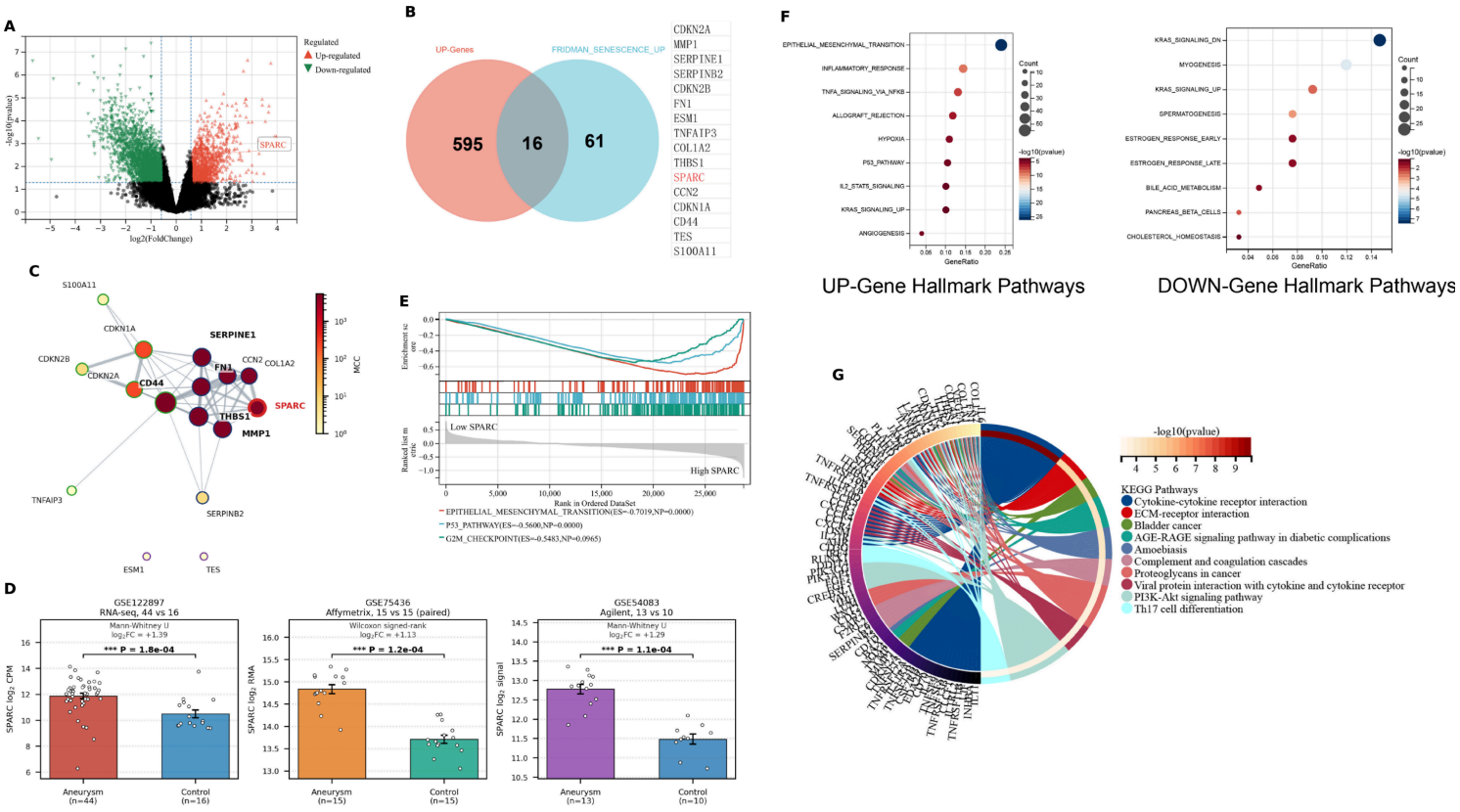


Figure 1

Differential expression and functional annotation in the GSE122897 intracranial aneurysm dataset. (A) Volcano plot for the control–IA comparison in GSE122897; SPARC is highlighted. (B) Venn diagram of up-regulated genes and the FRIDMAN_SENESCENCE_UP gene set. (C) STRING PPI network of the 16 overlapping genes. (D) SPARC expression in three independent datasets. (E) GSEA curves for selected Hallmark gene sets in samples ranked by SPARC expression. (F) Hallmark analyses of genes up-regulated and down-regulated in IA tissue, respectively. (G) KEGG pathway–gene chord diagram. Nominal P values are shown for GSEA in E.

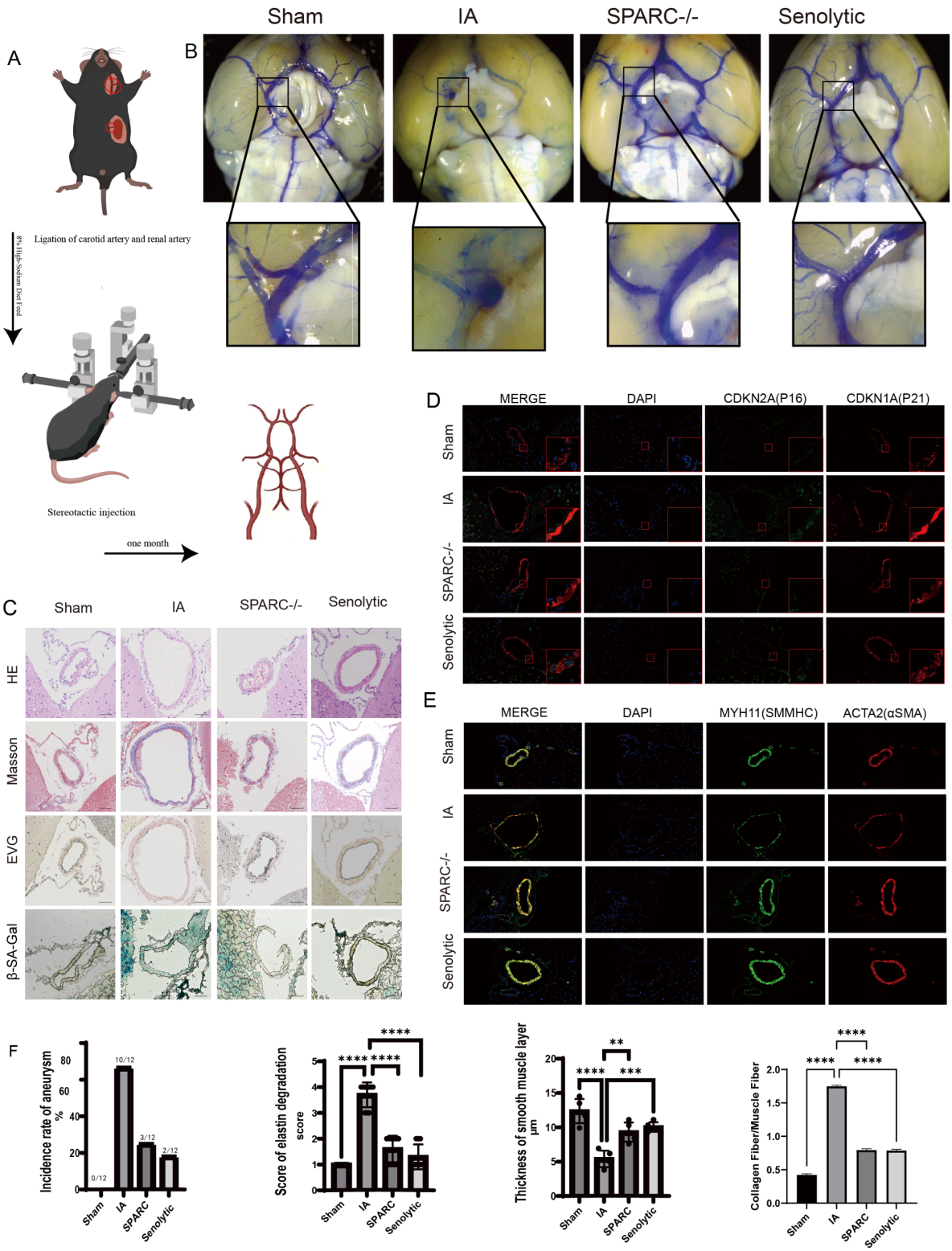


Figure 6

Arterial phenotypes after Sparc deficiency or senolytic treatment in mice. (A) Schematic of IA induction and tissue collection: unilateral carotid ligation and renal artery ligation, followed by stereotactic elastase injection, with tissues collected one month after induction. (B) Representative images of the Circle of Willis from sham, IA, Sparc$^{-/-}$ IA and D+Q-treated IA mice; insets show enlarged views of the boxed regions. (C) Representative H&E, Masson's trichrome, elastin–van Gieson (EVG) and SA-β-gal

staining of cerebral arteries. (D) Immunofluorescence for CDKN2A (p16; green), CDKN1A (p21; red) and DAPI (blue); the MERGE column shows the merged channels; insets show enlarged regions. (E) Immunofluorescence for MYH11 (SM-MHC; green), ACTA2 (α-SMA; red) and DAPI (blue). (F) Quantification of aneurysm incidence (0/12, 10/12, 3/12 and 2/12 for sham, IA, Sparc$^{-/-}$ and D+Q groups, respectively; Fisher's exact test), elastin degradation score, medial smooth muscle layer thickness and collagen fiber-to-muscle fiber ratio. n = 12 mice per group; 5 sections per animal and 3 repeated measurements per section were averaged to a single animal-level value.; each symbol represents one animal. *P < 0.05, **P < 0.01, ***P < 0.001, ****P < 0.0001 versus the IA group by Independent-samples t tests; n.s., not significant. D+Q, dasatinib plus quercetin.